Check for updates

Case History

Time-lapse walkaway vertical seismic profile monitoring for CO₂ injection at the SACROC enhanced oil recovery field: A case study

Di Yang[1], Alison Malcolm[2], Michael Fehler[2], and Lianjie Huang[3]

ABSTRACT

Geologic carbon storage involves large-scale injections of carbon dioxide into underground geologic formations. Changes in reservoir properties resulting from CO_2 injection and migration can be characterized using monitoring methods with time-lapse seismic data. To achieve economical monitoring, vertical seismic profile (VSP) data are often acquired to survey the local injection area. We investigated the capability of walkaway VSP monitoring for CO_2 injection into an enhanced oil recovery field at SACROC, West Texas. VSP data sets were acquired in 2008 and 2009, and CO_2 injection took place after the first data acquisition. Because the receivers were located above the injection zone, only reflection data contain the information from the reservoir. Qualitative comparison between reverse-time migration images at different times revealed vertical shifts of the reflectors' center, indicating the presence of velocity changes. We examined two methods to quantify the changes in velocity: standard full-waveform inversion (FWI) and image-domain wavefield tomography (IDWT). FWI directly inverts seismic waveforms for velocity models. IDWT inverts for the time-lapse velocity changes by matching the baseline and time-lapse migration images. We found that, for the constrained geometry of VSP surveys, the IDWT result was significantly more consistent with a localized change in velocity as expected from a few months of CO_2 injection. A synthetic example was used to verify the result from the field data. By contrast, FWI failed to provide quantitative information about the volumetric velocity changes because of the survey geometry and data frequency content.

INTRODUCTION

Public acceptance of geologic carbon storage as an effective and environmentally friendly solution to the mitigation of green house gas emission is a major prerequisite for the method to be widely implemented on the scale necessary to reduce the atmospheric CO_2 concentration. The injected CO_2 needs to be monitored over time to demonstrate that the fluid is contained within the targeted formation. It is also crucial to detect fluid migration in the subsurface and potential leakage to ensure safe and reliable storage (Bickle et al., 2007). CO_2 is usually injected into reservoirs such as saline aquifers and depleted oil and gas fields, which are predominantly water-saturated formations (Benson and Cole, 2008). The displace-

ment of water by CO_2 tends to reduce the bulk modulus and density of the rock-pore fluid system (Purcell et al., 2010). These properties determine wave speed changes that can be observed using seismic methods.

Time-lapse seismic monitoring is widely used in reservoir management in the oil industry to obtain information about reservoir changes caused by fluid injection and subsequent production of fluids from heterogeneous reservoirs. It helps identify bypassed oil to be targeted for infill drilling, and it extends the economic life of a field (Lumley, 2001). It is also capable of monitoring the progress of fluid fronts providing information for injection optimization in enhanced oil recovery (EOR) and long-term CO_2 sequestration.

Generally, one baseline survey and subsequent monitoring surveys are acquired over time. Qualitative analysis of time-lapse seismic data gives information about the temporal reservoir changes with amplitude maps and time shifts at certain horizons. Impedance contrasts and seismic response changes such as amplitude changes and tuning effects have been used to characterize CO_2 accumulations in thin layers, and velocity pushdown effects that are caused by slower propagation of seismic waves through the CO_2 saturated area have been identified (Arts et al., 2004a). Quantitative methods have also been proposed to directly deliver reservoir property changes such as pore pressure and fluid saturation by linking the rock-physics modeling, reservoir simulation, and 4D seismic response simulation (Landa and Kumar, 2011; Tolstukhin et al., 2012). However, these methods are conducted with poststack data or even 1D wave propagation, which focus on a local region and lose general information during the stacking process. For example, the time-lapse changes illuminated by the seismic waves from a certain angle could be indistinct in the stacked data. The amplitude changes are also not well preserved after stacking without an updated velocity model. Lumley (2010) proposes a high-resolution quantitative method to estimate the volume of CO_2 underground by combining 4D seismic, electromagnetic, gravity, and inSAR satellite data; however, time-lapse seismic is used to provide qualitative information in this process.

Full-waveform inversion (FWI) has the potential to estimate subsurface density and elasticity parameters quantitatively (Tarantola, 1984; Virieux and Operto, 2009), and it is becoming more feasible with increasing computing power. However, FWI often requires large-offset surveys and low-frequency data to resolve low wavenumber velocities. Large monitoring networks on land or on the seafloor have been successfully deployed for CO_2 monitoring (Aoki et al., 2013; Bakulin et al., 2013). For small pilot carbon sequestration projects, economic considerations mean that limited acquisition is generally used to monitor CO_2 injection. Vertical seismic profile (VSP) data have been acquired in a few carbon-sequestration demonstration projects (Daley et al., 2008). The vertical resolution of VSP data is typically higher than that of surface seismic data because VSP data contain higher frequencies than surface seismic data. Unfortunately, VSP survey geometry reduces the ability of FWI to resolve volumetric velocity changes. In this geometry, FWI tends to produce a reflectivity model like that obtained using least-squares migration. Between baseline and time-lapse surveys, amplitude changes can be transformed into reflectivity differences between images. Kinematic information is indicated by changes in the apparent depths of reflectors instead of direct measures of velocity changes. If a constraint that forces the locations of reflectors can be used in FWI, the velocity-depth bias would be removed. However, we did not find an efficient way to implement such constraints.

As an alternative to FWI, we apply an image domain wavefield tomography (IDWT) method (Yang et al., 2013) to time-lapse VSP data. Based on the assumption that the geology has not changed dramatically over time, both the baseline and time-lapse seismic data should be able to image the same area in the subsurface. If the correct velocity models are provided for both data sets, the reflectors should be at the same location assuming that reservoir compaction is negligible compared to the seismic wavelength. In an inverse problem setting, given a baseline velocity model, the time-lapse velocity anomaly can be resolved by matching the reflector locations in time-lapse images with those in the baseline image. The amplitude differences between images, which could be caused

by reflectivity changes, are not sensitive to the smooth (low-wavenumber) velocity perturbations in the inversion.

The goal of this paper is to investigate the practical capability of VSP reflection data for monitoring CO_2 injection. We first introduce the theory of the imaging and inversion methods that we apply to the time-lapse VSP data, including reverse-time migration (RTM), FWI, and IDWT. In the following sections, we describe the geologic background of the SACROC EOR site, the injection history, and the seismic data acquisition and processing. Images and models obtained from different methods are compared to demonstrate how they provide different types of information about changes in the reservoir. Preliminary interpretation is given about the mechanism of reservoir response to CO_2 injection and the CO_2 fluid migration at the SACROC EOR field.

METHODOLOGY

In this section, we briefly introduce the methods used in this study: RTM, FWI, and IDWT.

RTM

An RTM algorithm consists of three steps: (1) forward propagation of the source wavefield, (2) backward propagation of the receiver wavefield, and (3) application of the imaging condition. Wavefield extrapolation is conducted by solving the wave equation:

$$\frac{1}{c^2(\vec{x})}\frac{\partial^2}{\partial t^2}u(t,\vec{x}) - \nabla^2 u(t,\vec{x}) = S(t,\vec{x}), \quad (1)$$

where $u(t,\vec{x})$ is the wavefield at a spatial location $\vec{x}$ and time t, $c(\vec{x})$ is the P-wave velocity in the medium, and $S(t,\vec{x})$ is the source function. The image is constructed by the zero-lag crosscorrelation of the source wavefield $u_s(t,\vec{x})$ and receiver wavefield $u_r(t,\vec{x})$ at the image point as follows:

$$I(\vec{x}) = \int_0^T u_s(t,\vec{x})u_r(T-t,\vec{x})\mathrm{d}t. \quad (2)$$

The value of $u_s(t,\vec{x})$ is calculated by solving equation 1 with an estimated source signature $S(t,\vec{x})$, and $u_r(t,\vec{x})$ is computed by solving equation 1 with the data, reversed in time, as the boundary condition. More details about RTM can be found in Baysal et al. (1983) and McMechan (1983).

FWI

FWI minimizes an objective function formed from the difference between modeled data and field data:

$$E(m) = \frac{1}{2}\|u-d\|^2 = \frac{1}{2}\delta u^T \delta u, \quad (3)$$

where u and d are the waveform measurements from forward modeling, and the field experiment, respectively, and $\delta u = u - d$. The superscript T denotes the transpose, and m is the P-wave velocity model to be updated. The gradient of the objective function is derived by taking its derivative with respect to m, given by

$$\nabla_m E = \left\langle \frac{\partial u}{\partial m} \right\rangle^T \delta u. \qquad (4)$$

The gradient can be calculated efficiently by crosscorrelating the forward propagating wavefields from the sources with the back propagating residual wavefields from the receivers (Tarantola, 1984). The objective function can be minimized via, e.g., the Gauss-Newton or conjugate gradient methods. Because of the computation and memory cost of calculating the Hessian matrix (Sheen et al., 2006), we use the nonlinear conjugate gradient method because it does not require the Hessian matrix, and it has a better convergence rate than the steepest descent method (Rodi and Mackie, 2001). The model parameters are updated in each iteration according to

$$m_{i+1} = m_i - \alpha G_{i+1}, \qquad (5)$$

where G_{i+1} is the search direction defined by the gradient of the current step $\nabla_m E$ and the search direction of the previous step G_i (Rodi and Mackie, 2001). The parameter α is the step length obtained from a line search algorithm to reach the minimum cost for each iteration. We first apply FWI to the baseline data. The model that best approximates the wave events in the baseline data is used as the initial model in the inversion for the time-lapse data set. The differences between the inverted baseline and time-lapse models are then used as an estimate of the effect of CO₂ injections.

IDWT

Symes and Carazzone (1991) introduce the principle that if the background velocity is correct, the migrated images with neighboring shot gathers should show the reflectors at the same depth. In a time-lapse situation, if the subsurface interfaces have not changed in space or the changes are much smaller compared to the seismic wavelength (e.g., weak compactions), we can introduce a similar principle that if the time-lapse velocity model is correct, the time-lapse migration images should show the same structures at the same locations as the baseline migration images do. Hence, we apply IDWT to resolve volumetric time-lapse velocity changes. The cost function is very similar to equation 3, but in the image domain

$$J(m) = \frac{1}{2} \| I_{\text{baseline}}(\vec{x}) - I_{\text{time-lapse}}(\vec{x}) \|^2, \qquad (6)$$

where I_{baseline} is the migration image produced with the baseline data and velocity model and $I_{\text{time-lapse}}$ is the migration image produced with the time-lapse data and the velocity model that is being updated iteratively.

The gradient of the objective function can be efficiently calculated by two crosscorrelations:

$$\nabla_m J(m) = -\int_0^T \left(\frac{\partial^2 \lambda_s(t, \vec{x})}{\partial t^2} * u_s(t, \vec{x}) \right.$$
$$\left. + \frac{\partial^2 \lambda_r(T-t, \vec{x})}{\partial t^2} * u_r(T-t, \vec{x}) \right) dt, \qquad (7)$$

where $u_s(t, \vec{x})$ and $u_r(t, \vec{x})$ are the source and receiver wavefields used to form the time-lapse migration image $I_{\text{time-lapse}}(\vec{x})$ as in equation 2 and $\lambda_s(t, \vec{x})$ and $\lambda_r(t, \vec{x})$ are adjoint wavefields computed by solving equation 1 with adjoint sources. The adjoint sources are the multiplication of the image residual $I_{\text{baseline}}(\vec{x}) - I_{\text{time-lapse}}(\vec{x})$ and the wavefields $u_r(t, \vec{x})$ and $u_s(t, \vec{x})$ (Yang et al., 2013). Similar derivations can be found in Plessix (2006). We use the same nonlinear conjugate gradient method as used for FWI described above to update the model. The velocity difference is resolved as the image difference is minimized.

With RTM, we transform the traveltime changes in the two data sets into depth changes of the reflectors in the images. FWI inverts the amplitude and phase differences between the two data sets to obtain differences in reflectivity. Through IDWT, we transform the depth changes of the reflectors between the baseline and monitoring images into velocity differences between the two models. The amplitude differences between images are not sensitive to the low-wavenumber velocity perturbations, which makes IDWT focus on the kinematics. In the data application, we show the advantages and limitations of these methods for time-lapse walkaway VSP surveys.

SITE BACKGROUND OF SACROC

Geology and injection history

The SACROC EOR field is located in the southeastern segment of the Horseshoe Atoll within the Midland basin of west Texas. It is composed of several layers of limestone and thin shale beds representing the Strawn, Canyon, and Cisco Groups of the Pennsylvanian. The Wolfcamp shale formation of the lower Permian provides a low-permeability cap rock above the Pennsylvanian Cisco and Canyon Groups in the SACROC Unit (Han et al., 2010). The limestone is mostly calcite with minor ankerite, quartz, and thin clay lenses.

Hydrocarbons have been produced from the SACROC field using the solution gas drive mechanism since 1948 when the unit was discovered. To maintain the subsurface pressure level and also improve the fluidity of the oil within the reservoir, the field has been flooded with water since 1954 (Dicharry et al., 1973). Although the water injection facilitated oil recovery, tremendous reserves still remained in the field by the end of the water-flooding period. CO₂ injections were considered as the best tertiary recovery plan, and they were initiated in 1972. More than 175 million metric tons of CO₂ have been injected into the SACROC field, and about half of that amount is assumed to be sequestrated between depths of 1829–2134 ft below the surface (Purcell et al., 2010). As a part of the phase II project of the Southwest Regional Partnership for Carbon Sequestration, time-lapse walkaway VSP data were collected before and after the first CO₂ injection in this region that began in October 2008, in collaboration with Kinder Morgan, Inc. The purpose of this project is to study the combined EOR and CO₂ storage.

Figure 1 shows a map of the well distribution within the area of study. Red dots mark the wells from which we have logging data. The distribution of the wells with logs sample roughly a northeast–southwest trend. Green squares denote the two injection wells (56-4 and 56-6). The monitoring well (59-2) at the blue star is to the north of the injection wells. The black circle encloses an area of 1 km in radius. Injection well 56-6 is 350 m away from monitoring well
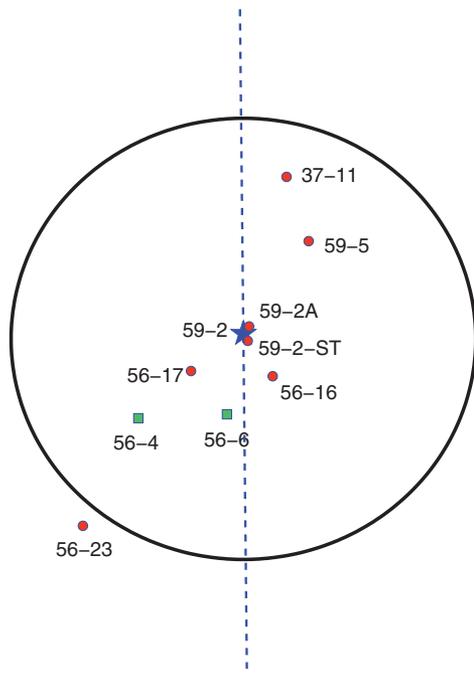
Figure 1. Schematic illustration of walkaway VSP surveys and CO_2 injection and monitoring wells at the SACROC EOR field. The red dots denote the wells with logging records. The green squares denote the two CO_2 injection wells. The blue star marks the VSP monitoring well where downhole receivers are installed. The black circle has a radius of 1 km. The blue dashed line is the walkaway VSP source line.
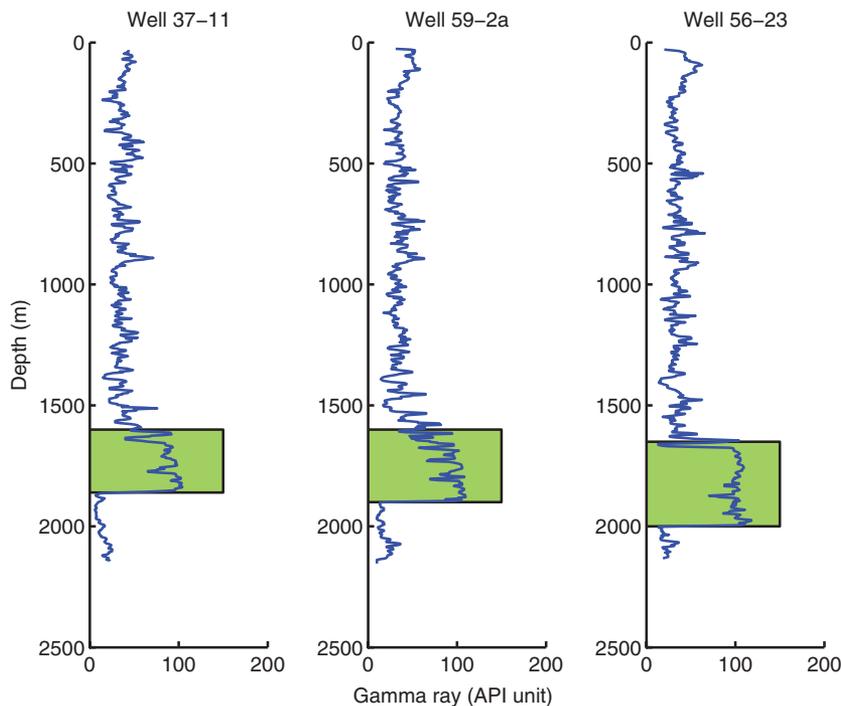
59-2. In between the two VSP surveys, CO_2 was injected in wells 56-4 and 56-6 at two intervals (centered at depths of approximately 1980 and 2040 m) (Cheng et al., 2010).

Well logs and reservoir properties

Well logs such as gamma ray, resistivity, and sonic velocity can be combined to verify the formation qualities within the range of interest. The gamma ray logs from wells 37-11, 59-2a, and 56-23 are shown in Figure 2. The interval with relatively high gamma ray values (green blocks in Figure 2) is interpreted to be a Wolfcamp shale formation, which is the cap rock for the CO_2 sequestration process. The wells in Figure 2 are along an approximate northeast–southwest trend through the injection wells. The shale formation gets slightly thicker and deeper toward the southwest.

Figure 3 shows resistivity, porosity, and sonic velocity logs in well 59-2a, which is close to the monitoring well. Combining all the readings in Figure 3 and the gamma ray log of 59-2a in Figure 2, we can estimate the thickness and depth of the shale formation at the well location. As indicated by the green blocks in Figure 3, the lower bound of the shale formation is at 1900 m, from where the reservoir formation starts. Low resistivity values indicate that very little organic matter remains in the reservoir and shale formations. At the interface between the shale and the limestone, there is a thin layer of high resistivity, which is interpreted to be residual gas. It is also proof of the good quality of the shale formation as a cap rock with very low permeability. The relatively high porosity (10% to 15%) of the limestone makes it a good candidate for CO_2 storage. Because the field has previously been flooded with water, the overall geology of the injection zone is comparable to a large class of potential brine storage reservoirs. The two injection intervals are located within the reservoir layer.

SEISMIC IMAGING AND INVERSIONS

Data acquisition and processing

The schematic configuration of the surveys is shown in Figure 4. The walkaway VSP source line is oriented along the north–south direction marked by a blue dashed line in Figure 1. It intersects the monitoring well location. Injection well 56-6 is slightly off the survey line. Two walkaway VSP data sets were acquired using the same well (59-2) in July 2008 and April 2009. The baseline data were acquired before the CO_2 injection that started in October 2008. Each survey consists of one zero-offset VSP, two far-offset VSPs (with offsets 1143 and 848 m), and one walkaway VSP. Vibrators were used as sources and were spaced at an interval of 37 m, with a total of 100 shotpoints. The data were collected in the monitoring well (59-2) using 13 receivers at depths ranging from 1555 to 1735 m, spaced at an interval of 15 m. Between the two surveys, CO_2 was injected through two injection wells (56-4 and 56-6 in Figure 1). We use the best-quality data from 97 shotpoints in this study.

Figure 2. Gamma ray logs from three wells: 37-11, 59-2a, and 56-23. Green blocks mark the interval of the Wolfcamp shale formations that have high gamma ray values.

The raw data sets were carefully processed by Cambridge Geosciences, Ltd. As illustrated in Figure 4, the downgoing waves do not contain any information from the reservoir because all the receivers are located above the reservoir layer. The downgoing waves and upgoing waves of the VSP data are separated using median filters (Cheng et al., 2010). We use the traveltimes of the downgoing waves to constrain the upper part of the velocity model. Static corrections are applied to compensate for the lateral heterogeneities of the weathered zone.

The amplitudes of upgoing waves in the 2009 data set are different from those in the 2008 data set. Based on the assumption that the geologic structures and physical properties have not changed above the reservoir (e.g., no earthquakes and compactions), the first reflection that is from the top of the shale formation should be identical in both data sets. Wang et al. (2011) conduct amplitude balancing on the common-receiver gathers of upgoing waves using the spectral ratios of the first wavelets (the first reflection). After the amplitude balancing, we align the first arrivals in the time-lapse data set with those in the baseline data set to eliminate traveltime inconsistencies.

Figure 5 shows the processed common-receiver gathers collected by the receiver at a depth of 1585 m. As expected, the first reflection signals from both data sets have the same amplitude and traveltime. The small time shifts of later events between two data sets are the time-lapse signal that we want to invert for velocity changes between the two surveys. There is no clear observation of new scattered waves in the time-lapse data. The dominant time-lapse effect is manifested by the small phase shifts.

We conduct our imaging and inversions in 2D space. The amplitudes of the data are compensated for the difference between 3D and 2D geometric spreading by applying a T-gain (multiply the data by $\sqrt{t}$ where t is time). In addition, the waveforms from 2D propagation contain a $\pi/4$ phase shift, so we adjust the phase of the data to ensure that there is no phase shift when comparing the synthetics to the data.

Initial velocity model

Because the shear waves are weak in the vertical components of the VSP data, all the methods we applied in this study use the acoustic assumption and so only the P-wave velocity model is used to propagate the data. We use a layered P-wave velocity model obtained from the zero-offset VSP data and sonic logging data to build the initial model. The 1D layered model and the sonic log at well 59-2 are shown in Figure 6. From the surface to the maximum depth of the zero-offset VSP receivers (which is 1737 m), we build a blocky layered velocity model using the direct wave traveltime at each zero-offset VSP receiver. For structures deeper than 1737 m, we use the sonic logging in well 59-2 to build a smooth velocity model by applying a moving average window as follows:

$$V(z) = \left(\sum_{i=z-w/2}^{z+w/2} \frac{1}{v(i)} \right)^{-1}, \qquad (8)$$

where w is the width of the moving average window, $v(i)$ is the sonic velocity value at depth of i m from the well log, and $V(z)$ is the averaged velocity at depth z. Here, w is 110 m, which is the
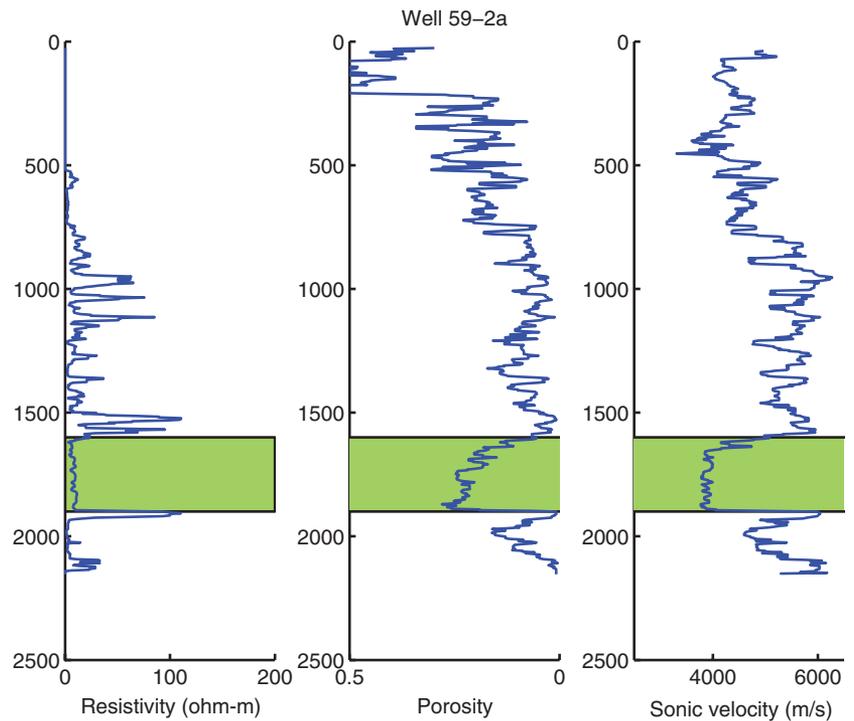
Figure 3. The resistivity, porosity, and sonic velocity profiles from the logging record at well 59-2a. Green blocks mark the interval of the Wolfcamp shale formation. The carbonate reservoir is beneath the shale formation. It is clear that the interface between the shale and the carbonate is at 1900 m.
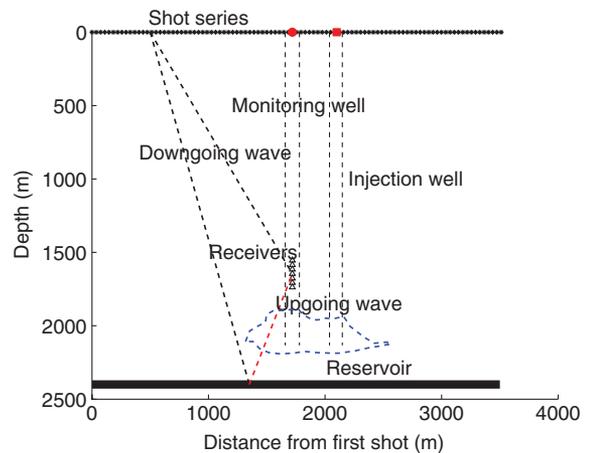
Figure 4. The schematic configuration of a VSP survey. The injection well is slightly out of the plane. Black and red dashed lines illustrate the downgoing (black) and upgoing (red) portions of paths for waves propagating from sources to receivers. The blue dashed line sketches the reservoir location.
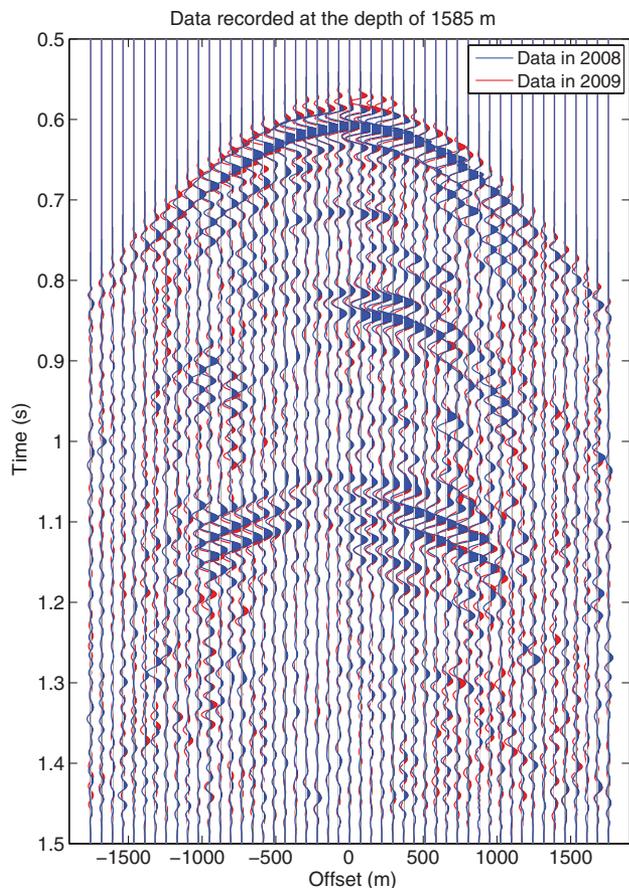
Figure 5. The processed common-receiver gathers of the data in 2008 (blue) and 2009 (red). The receiver is at 1585 m in well 59-2. The data sets are balanced in amplitude and traveltime using their first reflections. The traveltime differences in the later arrivals are the time-lapse-change signals.

P-wave wavelength at the data center frequency 45 Hz with 5000 m/s velocity. The logging profile only reaches a depth of 2134 m, which is still shallower than the depth where the strong reflections (around 0.8 s shown in Figure 5) occurred from below the reservoir. We linearly extrapolate the model beyond 2134 m. The density model is directly built from the density profile in the logging data.

RTM

Figure 7a and 7b shows the RTM images produced with the 2008 and 2009 data sets using the initial model. Two major features are clearly distinguished in both images: the interface between the shale formation and the reservoir and a deeper reflector. The location of the first reflector is at 1900 m, which is in agreement with the depth of the top of the reservoir inferred by the logging in Figure 3. The length of the first reflector in both images is about 200 m. The length of the second reflector at about 2300 m is about 600 m. There are several factors that contribute to this difference. First, the geometry of the survey results in the recording of reflections of a wider aperture from a deeper reflector. Second, we use only the vertical component of the 3C VSP data in this study. For a flat interface, it is clear that for P-waves, larger reflection angles lead to weaker vertical signals at the receiver. Third, some of the wave energy is converted to S-waves at the reflectors. The shallower reflector causes more conversion because of the larger reflection angle at the edges. All three effects combined give rise to weaker signals from the shallower reflector compared to those from the deeper reflector as offset increases as shown in Figure 5. RTM as a linear stacking process shows weaker reflectivity with weaker signals. That partially explains the significant difference between the lengths of the reflectors in our images; however, other amplitudes factors such as attenuation and the reflectivities as a function of angle may also contribute to the observed differences.

The location of the lower reflector in Figure 7b is shifted slightly downward compared to position in the image in Figure 7a. To
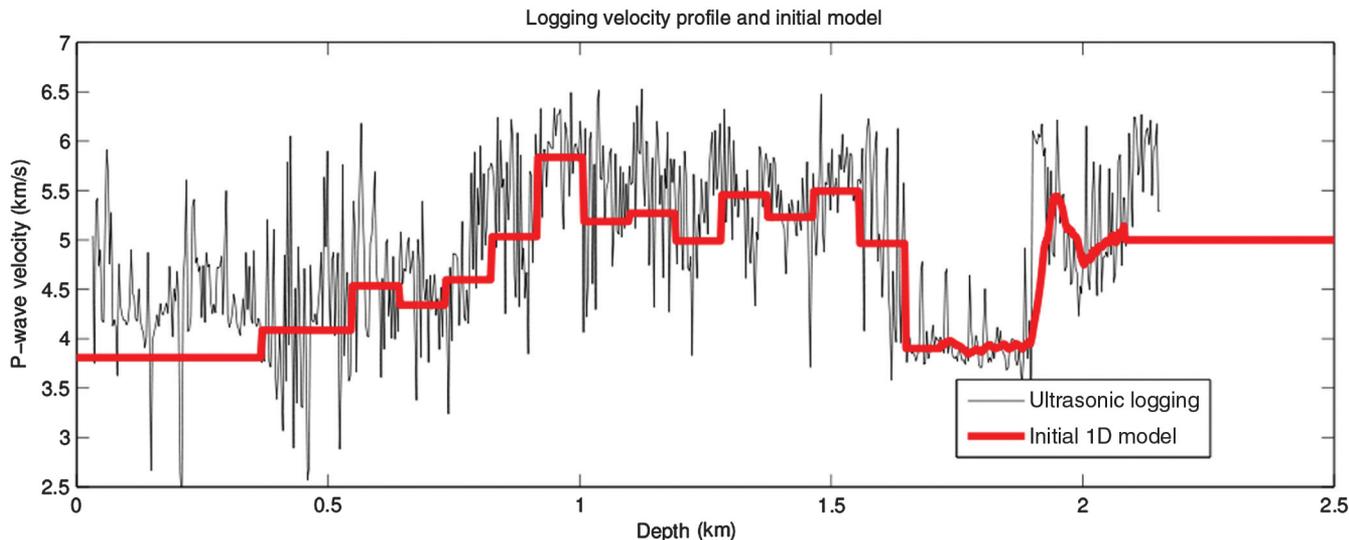

Figure 6. Black line: the sonic velocity profile from logging records in well 59-2a. Red line: the initial model built using the zero-offset VSP and the sonic velocity profile.

further investigate the shift, we plot a few columns of the images as traces in Figure 8, in which blue lines are from Figure 7a and red lines are from Figure 7b. The tops of the first reflectors are matched showing almost no shifts. The magnitude of the shift accumulates as the depth increases, and it plateaus below around 2100 m. This implies a velocity decrease below 1900 m during the time between the two VSP surveys.

Figure 9 shows a direct subtraction of the 2008 and 2009 migration images. The differences at the deeper reflector dominate the image. However, as demonstrated in Figure 8, the differences are caused primarily by the slight shifts between the two images. The bigger amplitudes of the deeper reflector lead to the bigger amplitudes in the image difference. It is misleading to interpret the subsurface changes directly from the image subtraction because the location of true subsurface changes is not directly linked to the location of the image differences. The differences below the reservoir due to the misalignment are because the time-lapse velocity model is not updated. In the following sections, we update the model using FWI and IDWT.

FWI

Before applying FWI to the data, we need to make a few assumptions. First, without a good estimation of the S-wave velocity model, we invert for only the P-wave velocity model. Second, the available data are measurements of the vertical components of the particle velocity measurements, so in the cost function (equation 3), we only minimize the differences between the vertical components of the synthetics and field data.

Starting from the model in Figure 6, we invert for the baseline model with the data from 2008. The result is shown in Figure 10a. Structures that are similar to those in Figure 7a are resolved. The lengths of the reflectors are extended compared to those in the migration images. The ratio of lengths between the shallower reflector

Figure 8. Sample traces from the RTM images of 2008 (blue) and 2009 (red). The lower reflectors in the 2009 image are shifted downward compared to the 2008 image.
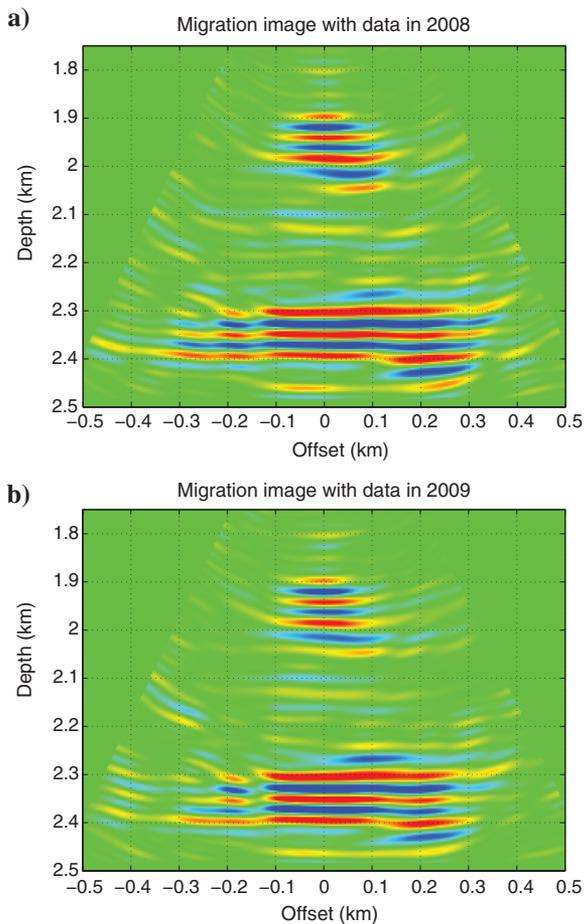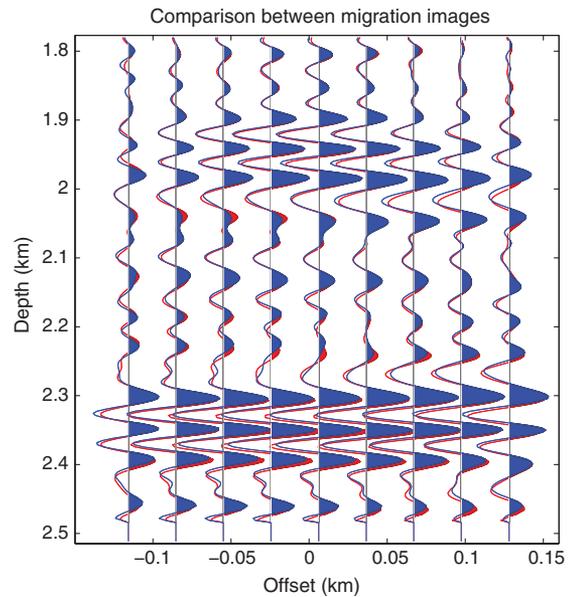

a)

b)

Figure 7. RTM images produced with data from (a) 2008 and (b) 2009. Both images show the local layered structures. The shorter reflector is at 1900 m, which is the top of the reservoir. For the 2009 image, the reflector below the reservoir is shifted slightly downward compared to the baseline image.
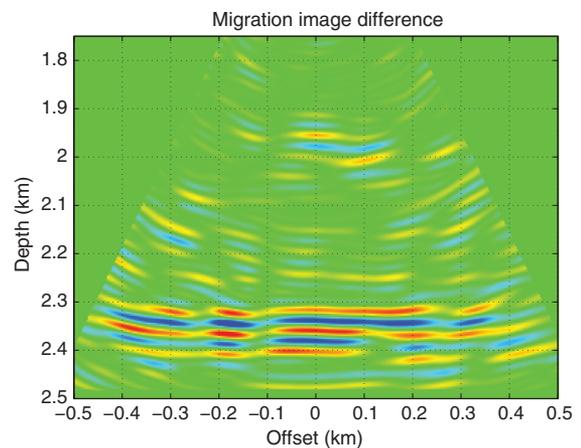

Figure 9. The image difference by subtracting the RTM image of 2008 from that of 2009. The changes at the deeper reflector are stronger than those in the reservoir layer.
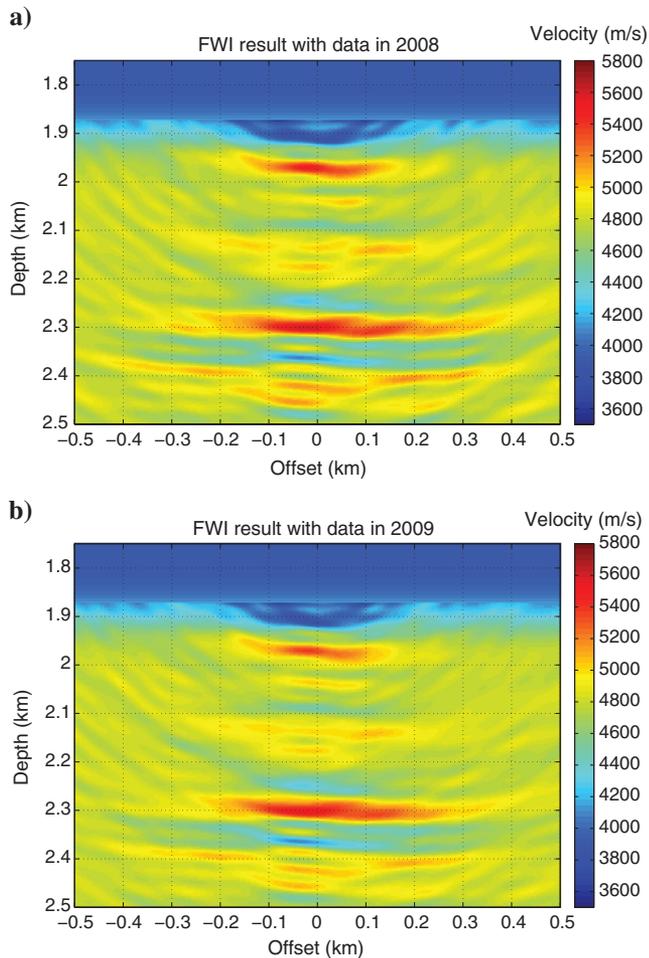
a)

b)

Figure 10. The P-wave velocity model reconstructed using FWI with data from (a) 2008 and (b) 2009. Both models contain similar structures. The 2009 model is shifted slightly downward compared to the 2008 model.
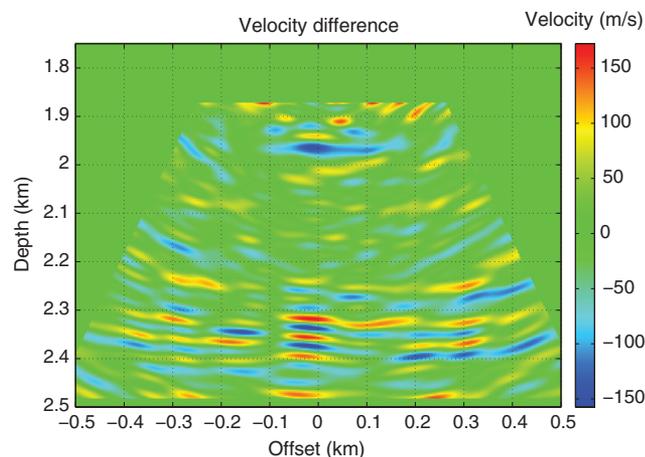

Figure 11. The P-wave velocity model difference obtained by subtracting the model of 2008 from that of 2009. The changes in the reservoir layer is comparable in amplitude with those at the deeper reflector. The changes are oscillating rather than smooth.

and the deeper reflector is increased, which is more reasonable for the migration image of a layered model. Unlike the linear stacking in migration, FWI compensates for the weak vertical components of the signals by taking into account the effects of the survey geometry and decreasing amplitudes with increasing reflection angle. In other words, the effect of the incomplete data (only vertical components) is mitigated in FWI.

One additional reflector at around 2100 m, which is interpreted to be the bottom of the reservoir formation, is clearly resolved. In the corresponding migrated image (Figure 7a), this reflector is visible but very weak in amplitude. This is because the reflectivities are not correctly balanced in RTM. By contrast, in FWI, the reflectivities are closer to true amplitude.

Although the image of the subsurface is markedly improved, FWI is not successful in resolving the smooth (low-wavenumber) velocity changes. Figure 10b shows the P-wave velocity model found using FWI on the data in 2009 and starting from the model obtained from the 2008 data. Similar to the RTM results, the 2009 model is a slightly downward shifted version of the 2008 model. Figure 11 shows differences in the models obtained by subtracting the 2008 model from the 2009 model. Compared to the image difference in Figure 9, the differences in the interval of 1900–2000 m and 2300–2400 m are comparable in amplitude. However, the differences are oscillating rather than smooth. With the walkaway VSP survey geometry, and only reflected waves used, FWI reduces to a least-squares migration that gives only a reflectivity model based on the background kinematics from the initial model (Plessix, 2006). The traveltime delay in the data is mapped to a depth shift rather than a velocity change in the inversion. With such small offsets and high-frequency data, the ambiguity between interval velocity and reflector depth is difficult to eliminate.

IDWT

From the migrated images, we estimate that the maximum depth shift is about 3 m. It is very unlikely that the reservoir would have compacted this much in between the two surveys (i.e., in 10 months) when oil production and CO_2 injection occurred simultaneously. The injection of CO_2 increases the pore pressure, preventing significant collapse of the reservoir rock. Moreover, if the reservoir top remains at the same location and the lower reflectors sink, as we observed in the migrated images, it actually means that the reservoir layer is stretched by 3 m, which is even more unlikely. Because the physical displacements of the interfaces are not expected to be this large, the traveltime delay is more likely caused by a P-wave velocity decrease. To invert the traveltime change for the amount of velocity change, we apply IDWT to the time-lapse walkaway VSP data from the SACROC EOR field.

Figure 12 shows the velocity changes resolved by IDWT. The most prominent feature is the low-velocity zone below 1900 m. It indicates that the CO_2 has probably migrated from the injection well toward the monitoring well. The top of the velocity changes is right beneath the cap rock. The initial injection was between depths of 1980 and 2040 m. It is possible that the CO_2 migrated upward because of buoyancy and accumulated at the bottom of the cap rock, resulting in local velocity changes. The length of the velocity anomaly is about the same length as the reflectors in the RTM images (Figure 7a and 7b). As described in the methodology section, IDWT inverts for velocity changes by matching the time-lapse reflection image with the baseline image. The extent of the recovered

velocity anomaly is constrained by the extent of the images. The area imaged in this survey is only around the monitoring well, which is about 350 m away from injection well 56-6. If what
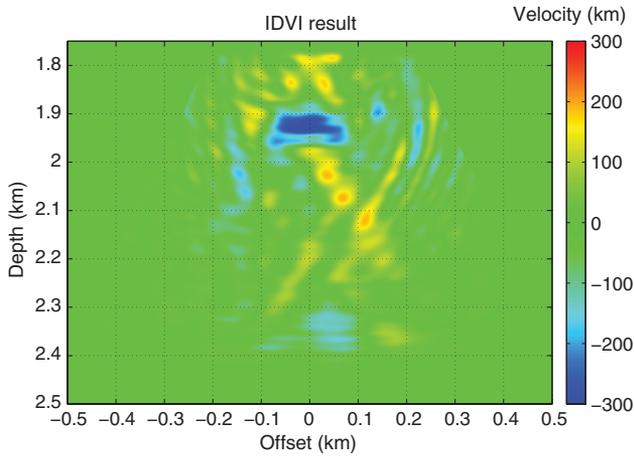
we resolve in Figure 12 is real, the velocity changes are spreading over the area between the two wells (59-2 and 56-6) because the reservoir formation is permeable and connected.

To verify the result in Figure 12, we use a synthetic example as a benchmark. The 1D layered model is used as the initial model to build the upper part of the synthetic baseline model (from 0 to 1500 m). From 1500 to 3000 m, we construct the layers according to the image in Figure 7a. Figure 13 shows the lower part of the model in which the low-velocity layer represents the shale formation. For the time-lapse model, we assume that a low-velocity anomaly is caused by the injected CO_2 flooding from the right side of the model to the area adjacent to the monitoring well as shown in Figure 14. Synthetic data are generated using finite-difference wave-equation modeling with the shot-receiver geometry exactly the same as that of the time-lapse walkaway VSP surveys at the SACROC EOR field. Figure 15 shows the RTM result with baseline data. Figure 16 shows the velocity anomaly reconstructed using IDWT. It is clear that the velocity changes are well bounded by the length of the reflectors and their vertical spacing. The velocity change to the right of the image is not recovered at all because of the acquisition geometry.

When the velocity is corrected using IDWT, the spatial shifts at the deeper reflector are eliminated. As a result, there are no anomalies present below the reservoir in Figure 16. In the SACROC case,
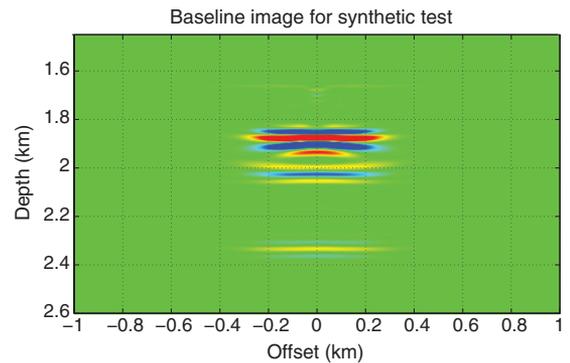

Figure 12. P-wave velocity changes reconstructed using IDWT. A smooth low-velocity zone is resolved within the reservoir. Some scattered velocity changes caused by image noise are also observed.

Figure 13. A synthetic layered model with the same geometry as the SACROC model. The blue layer is the shale formation, below which is the reservoir layer (red).

Figure 15. The baseline RTM image obtained using one common-receiver gather.

Figure 14. The synthetic P-wave velocity change caused by a fluid injection into a borehole located on the right side of the model.
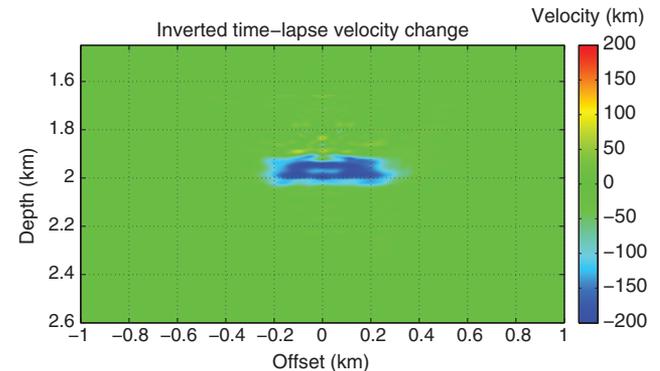

Figure 16. The P-wave velocity changes reconstructed using IDWT with the synthetic data. The low-velocity zone is confined within the reservoir and limited in width by the width of the reflectors in the image.

the velocity changes at the deeper reflector are significantly weaker compared to the strong differences in Figures 9 and 11. However, the inverted model is not as clear as the synthetic result. Several factors might contribute to these differences. One issue is the noise in the data. The time-lapse image is not an exact shifted version of the baseline image. Some differences between the images caused by noise are also minimized in IDWT, giving rise to the scattered velocity anomalies. Another issue is that the size of the low-velocity anomaly in Figure 12 is not big enough (limited width) to correct for all the shifting effects at the deeper reflector. Because of the acquisition geometry, some of the delay in the image is thus converted to local velocity updates. As a comparison, the velocity anomaly in the synthetic case (Figure 16) is wide enough to account for most of the deeper time delays. Hence, there are almost no anomalous velocity updates in the deeper part of the model.

DISCUSSION

The dominant time-lapse effect we observe in the time-lapse walkaway VSP surveys at the SACROC EOR field is a traveltime delay. Similar observations have been reported in several other papers (Arts et al., 2004a, 2004b; Daley et al., 2008). If the physical displacements of subsurface structures are relatively small, most of the traveltime delay is presumed to be caused by seismic velocity changes induced by the injections. There have been laboratory measurements of the velocity decrease of rock samples with different levels of CO_2 saturation (Purcell et al., 2010). If we are able to retrieve the velocity changes quantitatively, it will be possible to investigate fluid migration and the mineralization of CO_2.

To track the movement of the fluids, the time-lapse migration images can give qualitative information about the location of changes in the horizontal direction. As we observe from our RTM results, RTM converts a traveltime delay to a subsidence of the migration images beneath the top of the reservoir. It is inaccurate to use RTM images or image differences to interpret the changes in depth if the seismic velocity model is not updated after the injections.

Although FWI is considered an effective method of inverting seismic data for velocity models, in the SACROC walkaway VSP surveys, all the receivers are aligned in one monitoring well. For the area beneath the receivers, the ambiguity between depth and velocity is hard to reconcile without additional information. The FWI results with the SACROC VSP data are reflectivity models suffering from the same problems as RTM, despite the fact that the quality of the images is improved through the optimization process. Other downhole surveys such as crosswell and transmission VSP (Daley et al., 2008) have been successfully used to do tomographic inversions for CO_2 monitoring. If more monitoring wells are used, FWI may be capable of recovering tomographic velocity changes with VSP reflection data. Fewer receivers in two wells may

be better able to resolve tomographic changes than more receivers in a single well.

In this study, IDWT successfully resolves the P-wave velocity changes within the reservoir layer. It is also clear that the quality of the IDWT result depends on the quality of the migration images. FWI does improve the image quality; however, to use FWI as an imaging operator in IDWT is too computationally expensive. As we discuss in the RTM results section, the horizontal components of the particle velocity measurements can improve the image by compensating for small signal amplitudes from far offsets. To suppress the noise in the IDWT result, a preconditioning or filtering of the images might mitigate the influence of amplitude mismatches. Further research is needed to improve the performance of IDWT.

With the assumption that there is no compaction within the reservoir and the pore pressure stays approximately the same, we can give a rough estimation of the P-wave velocity change due to a simple fluid substitution using the Gassmann equation (Gassmann, 1951; Wang et al., 1998):

$$K_{sat} = K_{dry} + \frac{\left(1 - \frac{K_{dry}}{K_{min}}\right)^2}{\frac{\phi}{K_{fl}} + \frac{1-\phi}{K_{min}} - \frac{K_{dry}}{K_{min}^2}}, \qquad (9)$$

where K_{sat}, K_{min}, K_{dry}, and K_{fl} are the bulk moduli of the saturated rock, the forming minerals, the dry rock, and the fluid, respectively, and ϕ is the porosity. The density of the saturated rock is given by

$$\rho_{sat} = \rho_{fl}\phi + \rho_{min}(1 - \phi), \qquad (10)$$

where ρ_{sat}, ρ_{fl}, and ρ_{min} are the densities of the saturated rock, the fluid, and the forming minerals. If we assume a simple process of CO_2 replacing brine in the reservoir, the velocity change can be derived by changing values of K_{fl} and ρ_{fl} in equations 9 and 10. Based on the well log information, we obtained the parameters in Table 1. Then, the calculated P-wave velocity change is about 250 m/s, which is very close to our IDWT result.

To further link the velocity changes to quantitative measures of CO_2 content, production data and a good reservoir simulator should be used to calibrate the seismic inversion results and to obtain the reservoir parameters such as pore pressure and fluid saturation. Although we have not been able to do this here, it remains an important topic of future research.

CONCLUSIONS

We have applied the IDWT method to time-lapse walkaway VSP data acquired at the SACROC EOR field for monitoring CO_2 injection. Our inversion result shows a velocity decrease within a region beneath the top of the reservoir. This may indicate where the injected CO_2 migrated. For IDWT, data processing and balancing must be conducted carefully to suppress amplitude inconsistencies and preserve time-lapse signals. The high frequency of the data gives high image resolution, but the relatively small aperture limits the monitoring range. Neither RTM nor FWI is able to quantify the localized velocity changes, which are indicated by depth shifts of certain reflectors in RTM images and FWI results. IDWT can resolve a localized low-velocity

Table 1. Rock and fluid properties derived from well logs. Symbols are defined as in equations 9 and 10.

K_{min}	K_{dry}	K_{brine}	K_{CO_2}	ρ_{min}	ρ_{brine}	ρ_{CO_2}	ϕ
80 GPa	41 GPa	3.4 GPa	0.2 GPa	2.75 g/cc	1 g/cc	0.85 g/cc	10%

zone consistent with the geology and the injection pattern, which is interpreted to be the most likely change induced by the CO$_2$ injections.

ACKNOWLEDGMENTS

REFERENCES

Aoki, N., A. Takahashi, and Z. Xue, 2013, Development of a permanent OBC system for CCS monitoring in shallow marine environments: Energy Procedia, **37**, 4174–4181, doi: 10.1016/j.egypro.2013.06.319.

Arts, R., O. Eiken, A. Chadwick, P. Zweigel, B. van der Meer, and G. Kirby, 2004a, Seismic monitoring at the Sleipner underground CO$_2$ storage site (North Sea): Geological Society, London, Special Publications, **233**, 181–191, doi: 10.1144/GSL.SP.2004.233.01.12.

Arts, R., O. Eiken, A. Chadwick, P. Zweigel, L. van der Meer, and B. Zinszner, 2004b, Monitoring of CO$_2$ injected at Sleipner using time-lapse seismic data: Energy, **29**, 1383–1392, doi: 10.1016/j.energy.2004.03.072.

Bakulin, A., M. Jervis, R. Burnstad, and R. Smith, 2013, Making seismic monitoring work in a desert environment with complex near surface: 83rd Annual International Meeting, SEG, Expanded Abstracts, 4900–4904.

Baysal, E., D. D. Kosloff, and J. W. C. Sherwood, 1983, Reverse time migration: Geophysics, **48**, 1514–1524, doi: 10.1190/1.1441434.

Benson, S. M., and D. R. Cole, 2008, CO$_2$ sequestration in deep sedimentary formations: Elements, **4**, 325–331, doi: 10.2113/gselements.4.5.325.

Bickle, M., A. Chadwick, H. E. Huppert, M. Hallworth, and S. Lyle, 2007, Modelling carbon dioxide accumulation at Sleipner: Implications for underground carbon storage: Earth and Planetary Science Letters, **255**, 164–176, doi: 10.1016/j.epsl.2006.12.013.

Cheng, A., L. Huang, and J. Rutledge, 2010, Time-lapse VSP data processing for monitoring CO$_2$ injection: The Leading Edge, **29**, 196–199, doi: 10.1190/1.3304824.

Daley, T. M., L. R. Myer, J. E. Peterson, E. L. Majer, and G. M. Hoversten, 2008, Time-lapse crosswell seismic and VSP monitoring of injected CO$_2$ in a brine aquifer: Environmental Geology, **54**, 1657–1665, doi: 10.1007/s00254-007-0943-z.

Dicharry, R., T. Perryman, and J. Ronquille, 1973, Evaluation and design of a CO$_2$ miscible flood project-SACROC unit, Kelly-Snyder field: Journal of Petroleum Technology, **25**, doi: 10.2118/4083-PA.

Gassmann, F., 1951, Elastic waves through a packing of spheres: Geophysics, **16**, 673–685, doi: 10.1190/1.1437718.

Han, W. S., B. J. McPherson, P. C. Lichtner, and F. P. Wang, 2010, Evaluation of trapping mechanisms in geologic CO$_2$ sequestration: Case study of SACROC northern platform, a 35-year CO$_2$ injection site: American Journal of Science, **310**, 282–324, doi: 10.2475/04.2010.03.

Landa, J., and D. Kumar, 2011, Joint inversion of 4D seismic and production data: Presented at SPE Annual Technical Conference and Exhibition.

Lumley, D., 2010, 4D seismic monitoring of sequestration: The Leading Edge, **29**, 150–155, doi: 10.1190/1.3304817.

Lumley, D. E., 2001, Time-lapse seismic reservoir monitoring: Geophysics, **66**, 50–53, doi: 10.1190/1.1444921.

McMechan, G. A., 1983, Migration by extrapolation of time-dependent boundary values: Geophysical Prospecting, **31**, 413–420, doi: 10.1111/j.1365-2478.1983.tb01060.x.

Plessix, R.-E., 2006, A review of the adjoint-state method for computing the gradient of a functional with geophysical applications: Geophysical Journal International, **167**, 495–503, doi: 10.1111/j.1365-246X.2006.02978.x.

Purcell, C., A. Mur, Y. Soong, T. R. McLendon, I. V. Haljasmaa, and W. Harbert, 2010, Integrating velocity measurements in a reservoir rock sample from the SACROC unit with an AVO proxy for subsurface supercritical CO$_2$: The Leading Edge, **29**, 192–195, doi: 10.1190/1.3304823.

Rodi, W., and R. L. Mackie, 2001, Nonlinear conjugate gradients algorithm for 2-D magnetotelluric inversion: Geophysics, **66**, 174–187, doi: 10.1190/1.1444893.

Sheen, D.-H., K. Tuncay, C.-E. Baag, and P. J. Ortoleva, 2006, Time domain Gauss-Newton seismic waveform inversion in elastic media: Geophysical Journal International, **167**, 1373–1384, doi: 10.1111/j.1365-246X.2006.03162.x.

Symes, W., and J. Carazzone, 1991, Velocity inversion by differential semblance optimization: Geophysics, **56**, 654–663, doi: 10.1190/1.1443082.

Tarantola, A., 1984, Inversion of seismic reflection data in the acoustic approximation: Geophysics, **49**, 1259–1266, doi: 10.1190/1.1441754.

Tolstukhin, E., B. Lyngnes, and H. H. Sudan, 2012, Ekofisk 4D seismic-seismic history matching workflow: 74th Annual International Conference and Exhibition, EAGE, Extended Abstracts, 154347.

Virieux, J., and S. Operto, 2009, An overview of full-waveform inversion in exploration geophysics: Geophysics, **74**, no. 6, WCC1–WCC26 doi: 10.1190/1.3238367.

Wang, Y., L. Huang, and Z. Zhang, 2011, Reverse time migration of time-lapse walkaway VSP data for monitoring CO$_2$ injection at the SACROC EOR field: 81st Annual International Meeting, SEG, Expanded Abstracts, 4304–4308.

Wang, Z., M. E. Cates, and R. T. Langan, 1998, Seismic monitoring of a CO$_2$ flood in a carbonate reservoir: A rock physics study: Geophysics, **63**, 1604–1617, doi: 10.1190/1.1444457.

Yang, D., A. Malcolm, and M. Fehler, 2013, Using image warping for time-lapse image domain wavefield tomography: 83rd Annual International Meeting, SEG, Expanded Abstracts, 4926–4931.